iScience

CellPress
OPEN ACCESS

Article

Learning the stress-strain fields in digital composites using Fourier neural operator

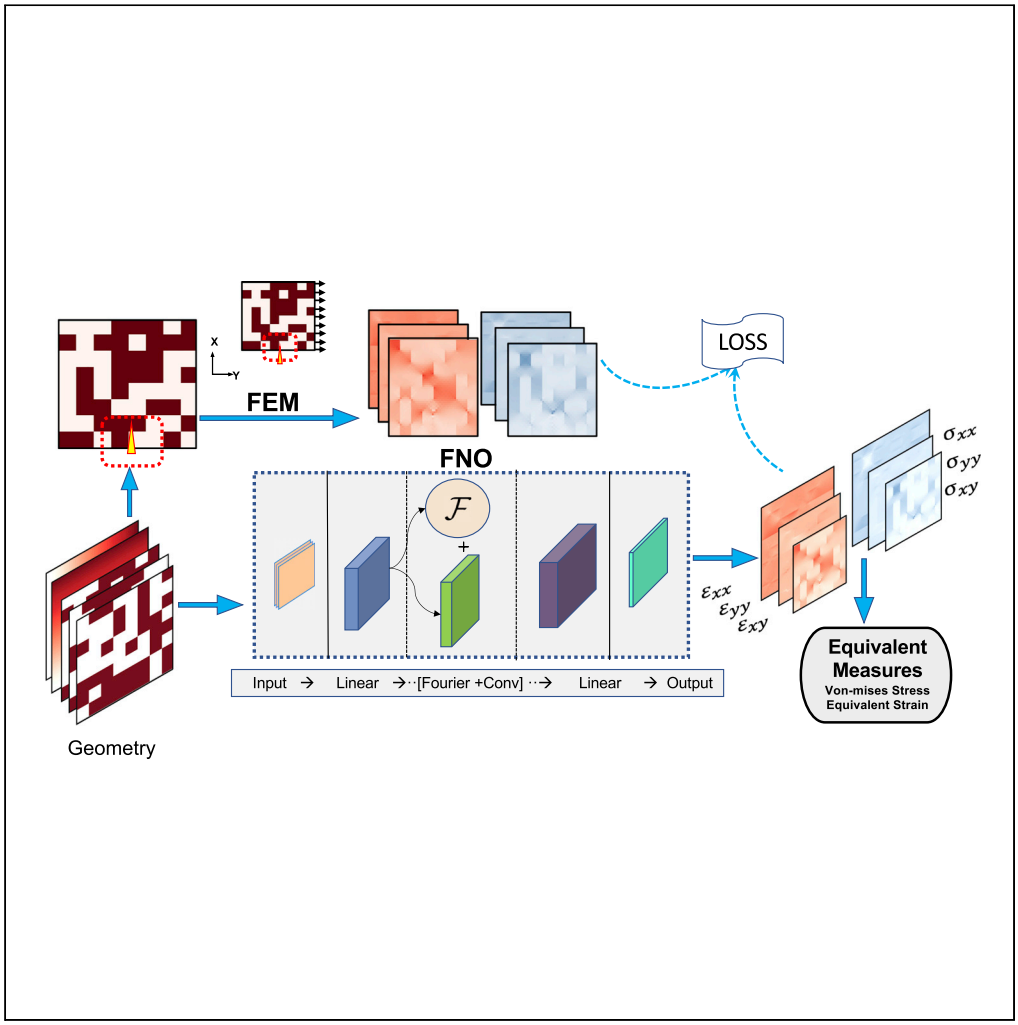

Meer Mehran Rashid, Tanu Pittie, Souvik Chakraborty, N.M. Anoop Krishnan

souvik@iitd.ac.in (S.C.)
krishnan@iitd.ac.in (N.M.A.K.)

Highlights

Predict stress and strain tensors directly from the microstructure

Demonstrate material and pixel-wise super-resolution of the FNO model

Zero-shot generalization to unseen arbitrary geometries

Measuring equivalent quantities such as von-mises stress and equivalent strains

Rashid et al., iScience 25, 105452
November 18, 2022
https://doi.org/10.1016/j.isci.2022.105452

iScience

CellPress
OPEN ACCESS

Article

Learning the stress-strain fields in digital composites using Fourier neural operator

Meer Mehran Rashid,[1] Tanu Pittie,[1] Souvik Chakraborty,[2,3,*] and N.M. Anoop Krishnan[1,3,4,*]

SUMMARY

Increased demands for high-performance materials have led to advanced composite materials with complex hierarchical designs. However, designing a tailored material microstructure with targeted properties and performance is extremely challenging due to the innumerable design combinations and prohibitive computational costs for physics-based solvers. In this study, we employ a neural operator-based framework, namely Fourier neural operator (FNO), to learn the mechanical response of 2D composites. We show that the FNO exhibits high-fidelity predictions of the complete stress and strain tensor fields for geometrically complex composite microstructures with very few training data and purely based on the microstructure. The model also exhibits zero-shot generalization on unseen arbitrary geometries with high accuracy. Furthermore, the model exhibits zero-shot super-resolution capabilities by predicting high-resolution stress and strain fields directly from low-resolution input configurations. Finally, the model also provides high-accuracy predictions of equivalent measures for stress-strain fields, allowing realistic upscaling of the results.

INTRODUCTION

The surging demands for high-performance materials with diverse functionalities necessitates accurate models for capturing the material response valid for a wide array of scenarios (Yang et al., 2021a, 2021b). Driven by the objective to engineer materials with tailored properties, such as stronger, lighter, and stiffer materials; researchers have resorted to combining multiple phases to arrive at a superior composite material that outperforms its constituent phases. Thus, while designing composites, the phase composition and microstructure are tuned to produce a mechanically superior material (Barbero, 2017) with desired properties and behavior. Many such advanced materials (bioinspired materials [Chen et al., 2012; Meyers et al., 2008; Su et al., 2020; Wegst et al., 2015; Gu et al., 2016b], meta-materials [Kadic et al., 2019; Liu and Zhang, 2011], architected materials [Meza et al., 2014, 2015; Pham et al., 2019; Zhang et al., 2020]) have been introduced with enhanced properties and performance. However, traditional manufacturing methods are incapable of exploiting material microstructure for improving the design due to difficulties in combining base materials. To fully harness the potential of material response, manipulations at the microstructural level have shown promise. In this regard, additive manufacturing has emerged as a feasible solution leading us to complex microstructural composites with unprecedented mechanical performance (Gu et al., 2016a).

In order to investigate the material behavior, various modeling methods at different length scales have been used such as finite element (Gu et al., 2016a) (FE), molecular dynamics (Chawla and Sharma, 2018; Kairn et al., 2005), or density functional theory (Zhou et al., 2019) simulations. Creating virtual models and subjecting them to different representative real-world settings is a prerequisite for understanding the behavior, design improvisation, and further development. However, the plethoric possibilities of material configurations make it almost impossible to navigate and arrive at the optimal design. Using the above-stated computational tools in conjunction with a brute force trial-and-error approach to analyze different geometries is not a feasible solution to optimize the design. Besides, these methods are exorbitantly expensive, lacking the means to transfer knowledge of one simulation to another. To address these drawbacks, recent advances in machine learning (ML) offer new solutions that are cost-effective and fast, as well as have transferability.

[1]Department of Civil Engineering, Indian Institute of Technology Delhi, Hauz Khas, New Delhi 110016, India

[2]Department of Applied Mechanics, Indian Institute of Technology Delhi, Hauz Khas, New Delhi 110016, India

[3]Yardi School of Artificial Intelligence, Indian Institute of Technology Delhi, Hauz Khas, New Delhi 110016, India

[4]Lead contact

*Correspondence: souvik@iitd.ac.in (S.C.), krishnan@iitd.ac.in (N.M.A.K.)

https://doi.org/10.1016/j.isci.2022.105452

Recent breakthroughs in ML have led to versatile algorithms perfectly modeling the complex nature of different scientific problems. With the advent of Graphical Processing Unit (GPU)- and Tensor Processing Unit (TPU)-facilitated ML and the abundance of data available, the training time has drastically reduced, paving way for highly advanced (Devlin et al., 2019; Ramesh et al., 2021; Senior et al., 2020) models solving intricate problems. The availability of ever-growing datasets has accelerated the advancements in ML, resulting in bigger and more complex predictive models with limitless parameters (Fedus et al., 2022) that exhibit immense expressive power. The promise shown by the ML methods has led researchers from different domains to embrace and employ ML in their respective fields. For material science, ML models have provided a cheap alternative to resolve difficult challenges and achieve high-fidelity results ergo facilitating computationally sophisticated research work. The application of ML techniques, particularly deep learning (DL) models, has facilitated novel material designs and accelerated material discovery, material modeling, and property predictions (Butler et al., 2018; Hughes et al., 2019; Jensen et al., 2019; LeCun et al., 2015; Qin et al., 2020).

Many studies (Cui and Chew, 2022; Ferreño et al., 2021; Stoll and Benner, 2021; Xie et al., 2021) have focused on predicting the mechanical properties of different materials. By using two convolution neural network (CNN) framework-based architectures—SCSNet (single-channel stress prediction neural network) and StressNet—to encode the structure, boundary condition, and external forces, Nie et al. (2019) predicted the von-mises stress fields for 2D elastic cantilever structures. Sun et al. (2020) used StressNet to predict the stress field in 2D slices of segmented tomography images of a fiber-reinforced polymer specimen. Yang et al. (2020) combined principal component analysis with CNN to predict the stress-strain behavior of the binary composite over the entire failure path. Liu et al. (2015) predicted microscale elastic strains in a 3D voxel-based microstructure volume element. Sepasdar et al. (2021) formulated a CNN-based framework to estimate the post-failure full-field stress distribution and crack pattern for a carbon-fiber-reinforced polymer composite. Similarly, Bhaduri et al. (2022) considered the U-Net architecture to map fiber configurations to von-mises stress fields. CNN becomes a natural choice when the solution is the image representation of any quantity due to its inherent capacity to detect local and global patterns. However, other DL-based networks such as recurrent neural networks (RNNs) and generative models have also been utilized to estimate the mechanical response of materials. Mozaffar et al. (2019) used RNNs to predict the plastic behavior of the composite representative volume element. Various studies suggest generative models (Hanakata et al., 2020; Kim et al., 2020; Lim et al., 2018) while addressing the inverse problem of finding the potential material based on target properties. Furthermore, Yang et al. (2021a) used condition generative adversarial network (cGAN) to predict the stress-strain fields for random two-phase microstructures. Besides, the results are used to derive secondary material properties. In a different work, the authors (Yang et al., 2021b) use cGAN to predict the multiple tensorial stress-strain components. However, most of the models suffer in generalization, thereby failing to make predictions for the input settings unseen to the model. While predicting stresses or strains, the existing studies predict a single tensorial component. Even though Yang et al. (2021b) predicted multiple components, each tensor element is predicted by a different trained model, thereby making it computationally expensive to predict a full tensor. Additionally, such pixel-to-pixel learning-based methods are incapable of resolving higher-resolution inputs unseen during model training.

To address these drawbacks, we use the Fourier neural operator (Li et al., 2021) (FNO) to predict component-wise stress and strain for two-phase composites. Using the microstructure of the material alone as an input, we predict the normal and shear components of the stress and strain tensor field in an end-to-end fashion. The model learns the relation between the design geometry and material response with high accuracy. By predicting the stress and strain tensors, the model learns the constitutive relation purely from data, devoid of any knowledge of the underlying physics of the problem. We demonstrate the ability of the ML model to generalize to unseen geometries with arbitrary shapes. Also, the super-resolution feature of the FNO model allows high-resolution output for low-resolution inputs. Using the stress and strain predictions, we also show that equivalent stress- and strain-based quantities, viz, von-mises stress and equivalent strains, can be estimated with high-accuracy, allowing upscaling of the results to higher-length scales.

RESULTS

FNO framework

First, we briefly discuss the FNO-based framework used to predict the nonlinear stress-strain response for the 2D hierarchical composite. Figure 1 presents the graphical workflow followed in this study. We consider a

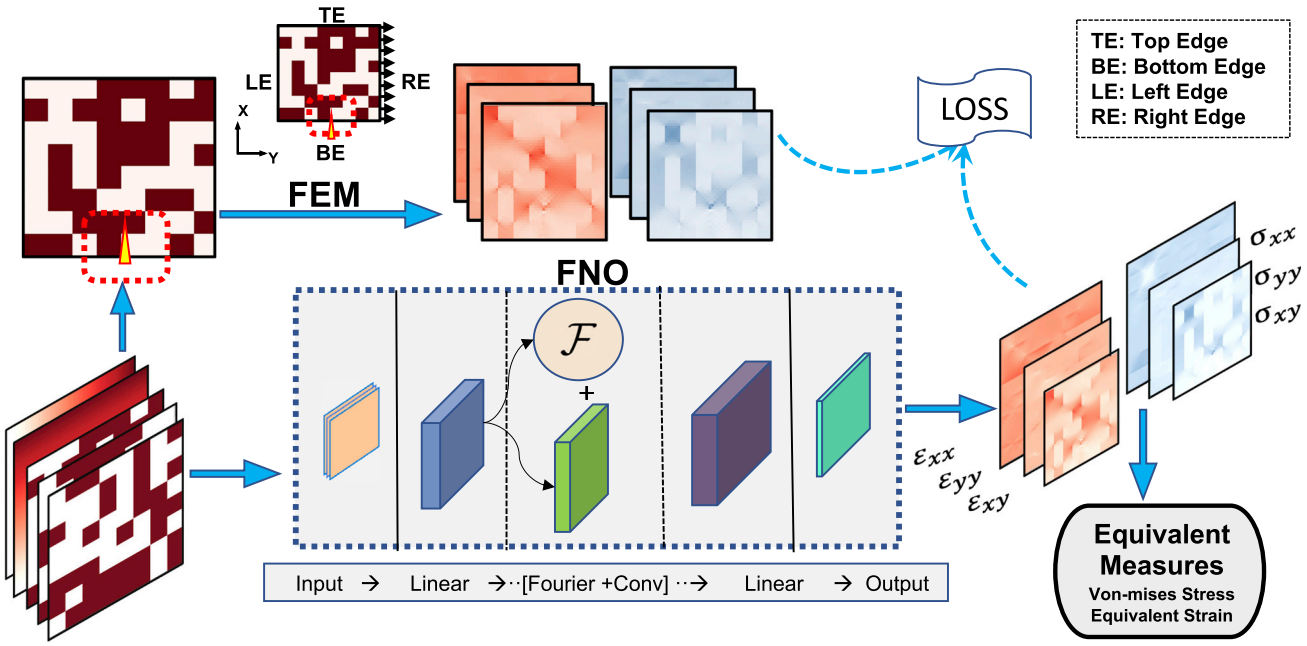

Figure 1. Workflow

The 2D digital composite geometry is analyzed for the mode-I tensile test using FEM. Pre-crack is along the x-direction, and loading is applied in the y-direction. This simulation is done to establish the ground truth for model training. Material geometry image is the input to the FNO model. The FNO framework used has 6 layers; 2 linear layers and 4 Fourier layers. The model is trained separately to predict stresses and strains (Figure S3), but for each of these field variables, all the components are predicted in a single pass. The trained model outputs are validated against the accurate FEM results besides testing it for unseen geometries. The tensor components are used to derive scalar-valued equivalent measures such as von-mises stress and equivalent strains.

binary composite, i.e., a composite consisting of two arbitrary materials of different stiffness. The initial geometry is generated in a checkered pattern, with each square randomly assigned one of the two materials. Ground truth is generated using FE simulations (see method details). The randomly generated geometric configurations are given as input to the FNO model to predict the stress-strain response of the material by operator learning in a supervised fashion, where the ground truth is extracted from the FE simulations.

Specifically, we use the FNO to learn the constitutive relation for the digital composite by predicting the component-wise stress and strain fields. FNO belongs to the recently established neural operator class of DL frameworks that are used to model a wide range of complex problems (mainly governed by Partial Differential Equations-PDEs), e.g., turbulent flows, multiphase flow, and weather predictions. The parameters are learned in the Fourier space where the output of each Fourier layer is truncated by dropping higher Fourier modes mainly responsible for details of the construction. Broadly, FNO as shown in Figure 2, comprises a lifting layer, iterative kernel integration layers or the Fourier layers, and the projection layer. The input is lifted to the higher dimension using a lifting layer P, essentially a linear layer with 32 nodes in our case. The higher dimensional output goes through an iterative setup of Fourier layers, and within each Fourier layer, the physical representation is convoluted with the kernel function, which amounts to simple multiplication in the Fourier space. FNO utilizes the FFT algorithm to transform both the entities followed by product operation. The output is filtered by removing the higher modes, thereby neglecting the high-frequency noise in the feature information. This filtration leads to the model speed up as well as model generalization. FNO uses the inverse FFT to transform back these filtered modes to the spatial domain. Finally, the output of these Fourier layers is projected to the target dimension using the projection layer Q, which is a linear layer with 128 nodes. Further details of FNO used in the present work are provided in the method details section.

Stress-strain prediction

The general stress-strain relationship (generalized Hook's law) is defined as

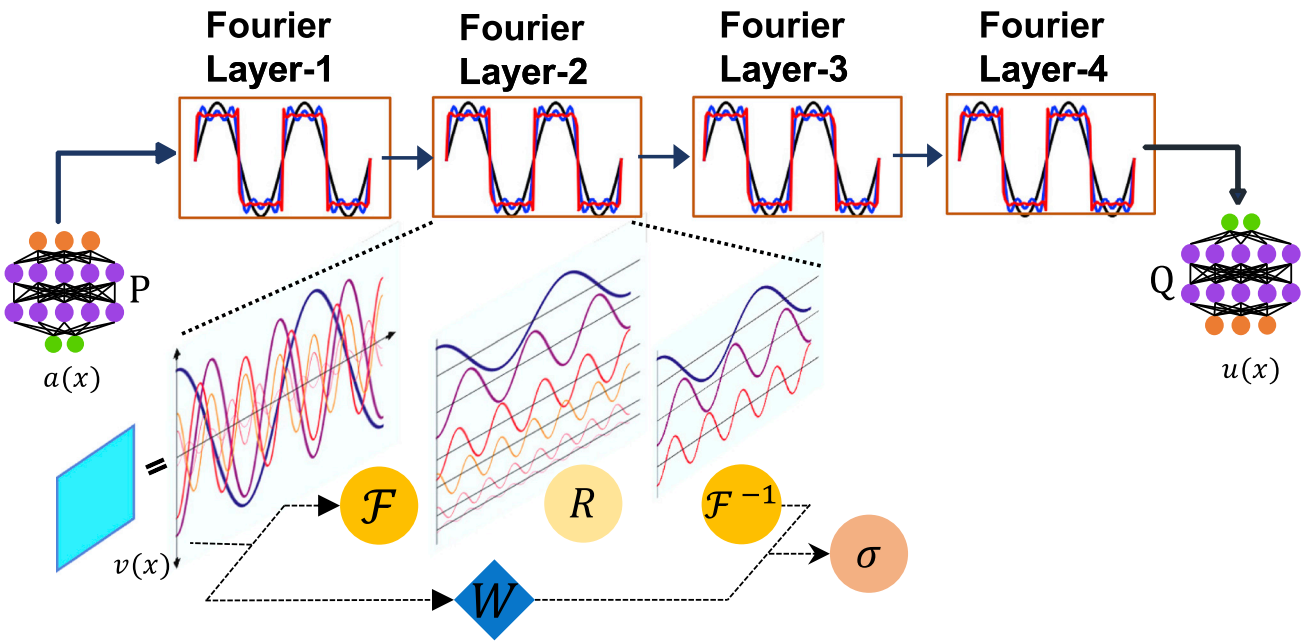

Figure 2. Fourier Neural Operator-FNO network architecture

The input is lifted to the higher dimensional channel space through a neural network P. The output of this linear layer is fed iteratively to the 4 Fourier layers. Each Fourier layer is an integral convolution in Fourier space. Taking the Fourier Transform $\mathcal{F}$ of the input $v(x)$, followed by a linear transformation R on the lower modes and truncating higher modes, and then applying inverse Fourier Transform $\mathcal{F}^{-1}$. Besides, the input is concurrently supplied to the local linear transformation W. The combined output of the spectral layers and convolution layer is acted upon by a nonlinear activation function σ. Finally, the neural network Q projects the output back to the target dimension. $u(x)$ is the solution prediction of the FNO.

$$\{\sigma_{ij}\} = C_{ijkl}\{\varepsilon_{kl}\} \quad \text{Equation 1}$$

where σ_{ij} and ε_{kl} are the stress and strain components, respectively, and C_{ijkl} is the overall stiffness tensor. For 2D problem, we have $\sigma_x, \sigma_y, \sigma_{xy}$ satisfying the stress-equilibrium equations as:

$$\frac{\partial \sigma_x}{\partial x} + \frac{\partial \sigma_{xy}}{\partial y} + F_x = 0 \ (\text{along x} - \text{axis}) \quad \text{Equation 2}$$

$$\frac{\partial \sigma_y}{\partial y} + \frac{\partial \sigma_{xy}}{\partial x} + F_y = 0 (\text{along y} - \text{axis}) \quad \text{Equation 3}$$

where F_x and F_y are the body forces in x and y directions, respectively,

and strains $\varepsilon_x, \varepsilon_y, \varepsilon_{xy}$ defined as

$$\varepsilon_x = \frac{\partial u_x}{\partial x}, \ \varepsilon_y = \frac{\partial u_y}{\partial y}, \ \varepsilon_{xy} = \frac{\partial u_x}{\partial y} + \frac{\partial u_y}{\partial x} \quad \text{Equation 4}$$

where u_x and u_y are the displacements in the x and y directions, respectively.

In this study, we use the FNO framework to estimate the stress and strain components for the 2D tensile problem. By learning the distinct tensor components, we demonstrate the ability of the FNO to learn the underlying constitutive relationship for the 2D composite from the material geometry grid (each grid point in the input material geometry image has an E value of the corresponding FE element).

To demonstrate the ability of FNO to predict complex stress-strain patterns, we train the model with the data on the mode-I quasistatic fracture response of a digital composite (Figure 1) having soft and stiff units (see Table 1 for material properties) . For each material geometry, the model predicts three stress components, viz, σ_{xx}, σ_{yy}, and σ_{xy}, as well as three strain components, ε_{xx}, ε_{yy}, and ε_{xy}. The FNO-based stress-strain predictions for a typical composite are shown in Figure 3. Unlike the previous studies (Yang et al., 2021b), our model

Table 1. Material properties of arbitrary 2-phase composite

Property	Soft material	Stiff material
Modulus of elasticity (E) (MPa)	100.00	1000.00
Poisson's ratio	0.33	0.33
Failure strain (ε)	0.4	0.04
Fracture energy (G) (0.5 × E× ε^2 × volume)	0.008	0.0008

predicts full stress-strain tensors in a single pass. Instead of training different models for each component, we just train two models to predict all the components of the stress and strain tensor. The model input is the material geometry image having 8 × 8 material units and 48 × 48 image resolution. Figure 3A reveals the component-wise stresses compared to the Finite Element Method (FEM)-based ground truth. The output field maps for each component are also 48 × 48. The predicted strain fields qualitatively and quantitatively agree with the ground truth except in the regions of the crack tip and a rare occurrence at the soft-stiff unit interface. It is important to mention that calculating a single value-based error for the whole image does not provide insight into the accuracy of the results. In order to quantitatively evaluate the accuracy of the model predictions, we calculate the pixel-wise absolute error (AE) and absolute relative error fractions for each component. Only a few pixels show relatively high error; this is due to the development of localized stress concentrations at and around such regions. For the rest of the grid points, the results are consistent with the FEM output and precisely capture the stress patterns for each component. As expected, relatively higher stress values are generated in stiffer units. It can be visualized clearly in the stress distribution maps, especially for the σ_{yy} component, as the loading is applied in the y-direction. Similarly, Figure 3B shows the three strain component predictions that are obtained from a different trained model. The strain field predictions exactly resemble the ground truth (FEM results). The exactness of global strain patterns for composite geometry is remarkable, especially the ability to pick up the crack tip position besides the complex response at soft-stiff unit interfaces. The difficulties in model predictions at the crack tip are expected since this represents a discontinuity that is even challenging for conventional solvers. Creating a DL framework with the capacity to exactly capture the crack behavior is a potential area for future work.

Now, we plot the results along cross-sections in two specific directions to further illustrate the accuracy of the model predictions for stress and strain components. We choose two lines, *XX* and *YY*, along the horizontal and vertical directions, respectively, and plot the model predictions vs. ground truth (FEM) for each of the tensor components. Figure 4 shows the results for one such example wherein for the same material geometry, we show stress components σ_{xx}, σ_{yy}, and σ_{xy} in Figure 4A and strain components ε_{xx}, ε_{yy}, and ε_{xy} in Figure 4B. The results almost precisely match the ground truth, thereby capturing the complex nature of these quantities. Except the boundary and regions around the crack tip, FNO yields precise results with predictions overlapping the FE results. This is valid for any component of stress or strain tensor evaluated by the model. With such accurate predictions, the model can be used to achieve high-fidelity results for field quantities, thereby enabling us to explore the design landscape as well as comprehensively understand the material behavior.

To compare the FNO results with standard existing CNN-based DL models, we choose ResNet (He et al., 2015) and U-Net (Ronneberger et al., 2015) models to evaluate the tensor components for both the physical quantities considered. We evaluate these models for the same 200 test samples, and the results are shown in Table 2. We measure the R^2 values as well as the L_2-based error defined as:

$$\mathcal{L}_2 = \frac{\sqrt{\sum_{i=1}^{m}(u(x_i) - \hat{u}(x_i))^2}}{\sqrt{\sum_{i=1}^{m}(u(x_i))^2}} \qquad \text{Equation 5}$$

where $u(x_i)$ is the ground truth and $\hat{u}(x_i)$ is the pixel-wise model prediction for the *i-th* point. The results demonstrate the superior performance of the FNO framework in predicting both the stress and strain components.

Material and pixel-wise super resolution

Until this point, the models have been trained on the input material geometry image of 8 × 8 grid of soft and stiff units, and the overall image resolution for the input and output image maps was 48 × 48. The

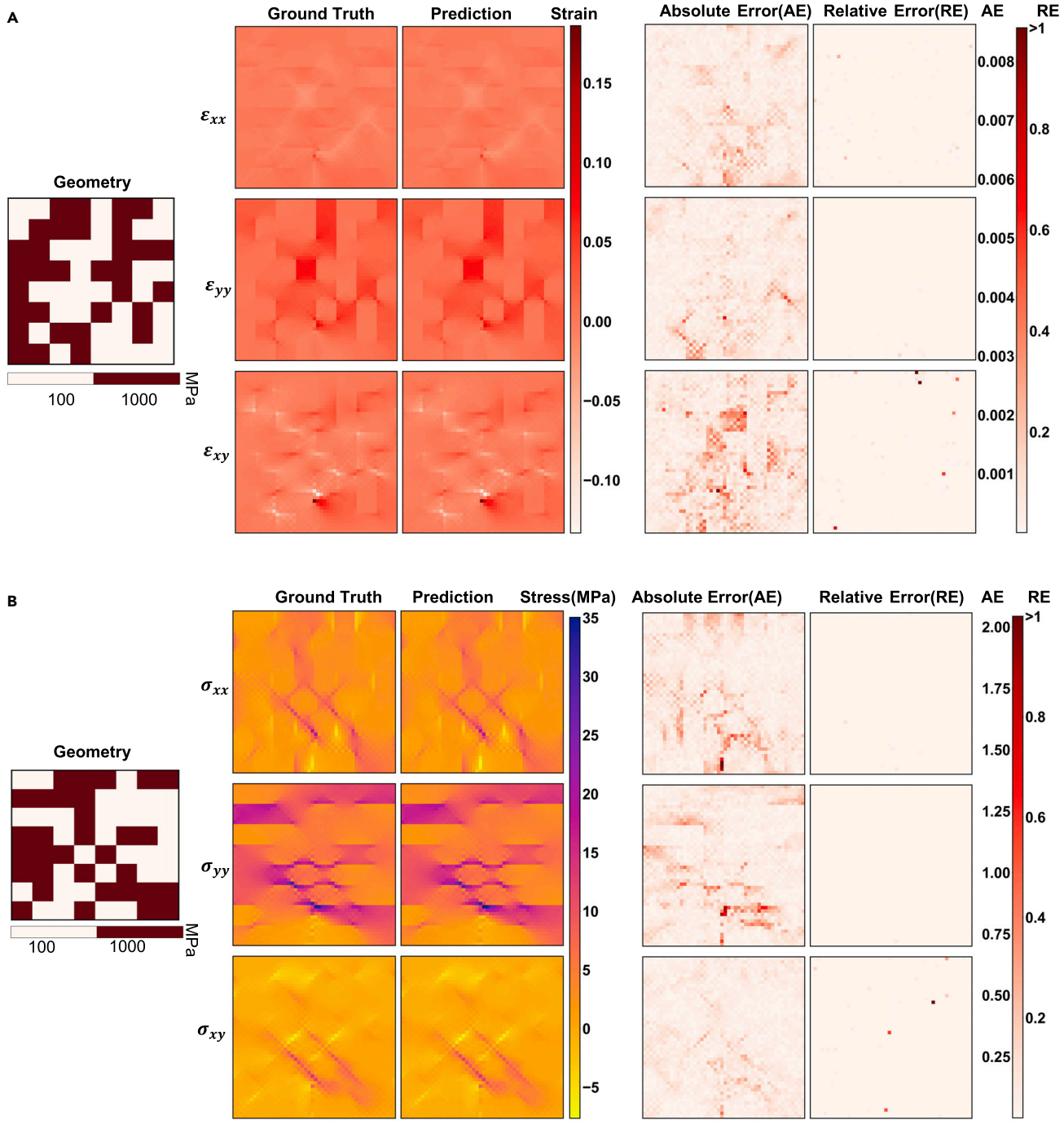

Figure 3. Component-wise stress-strain prediction maps by the ML model for the 2D composite compared to high fidelity FEM solution

(A) FNO predicting the three stress components σ_{xx}, σ_{yy}, and σ_{xy} for a typical composite material. The stress distribution is compared to the ground truth. Pixel-wise absolute relative error (AE) and absolute relative error (RE) maps are also shown corresponding to each stress component.

(B) Similarly, predictions of strain components ε_{xx}, ε_{yy}, and ε_{xy} by the model compared with the FEM results. AE and RE maps for point-wise error quantification.

material resolution of 8 × 8 represents a simpler material configuration, but the geometries are more complex in real-world applications, and a higher material grid resolution is observed. To address this challenge, we exploit the super-resolution capability of FNO, both in spatial as well as temporal domains. The model trained on lower-resolution data can be evaluated for higher resolution, making

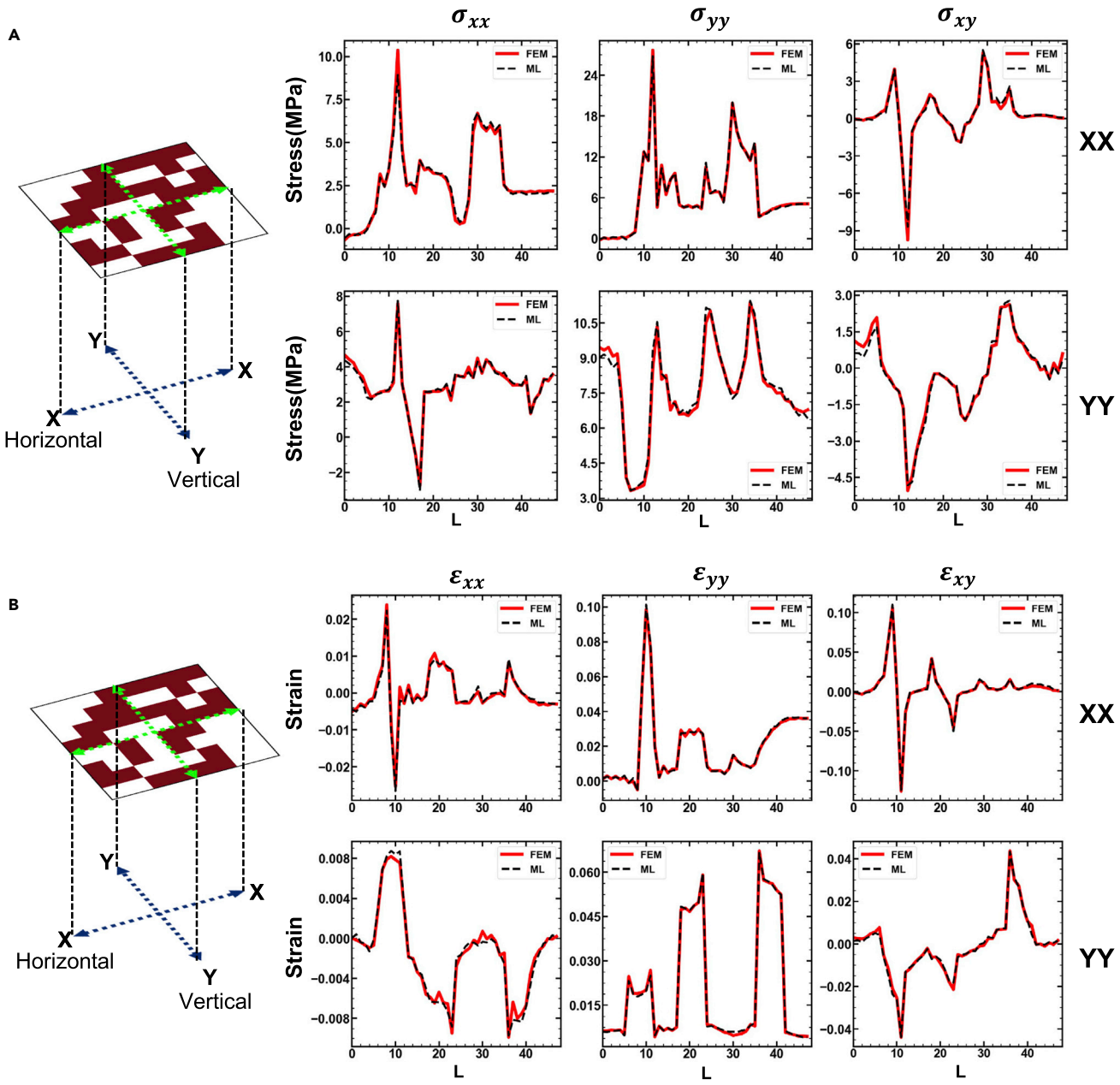

Figure 4. Quantitative comparison of tensorial components along the specific cross-sectional directions

(A) Comparison of stress values for each component along the *XX* and *YY* directions.

(B) Comparison of strain values for each component along the *XX* and *YY* directions.

FNO discretization invariant. Unlike classical solvers whose results are significantly affected by the size of discretization, FNO is able to transfer the solution from lower resolution to higher resolution. This is possible because FNO by design learns the parameters, which are the Fourier modes in Fourier space. We exploit this feature and use the trained model to evaluate stress and strain fields on higher-resolution images. For the case of material super-resolution, we test the model with input geometries having a 16 × 16 material grid and 96 × 96 overall image resolution. The model predictions are shown in Figure 5A depicting the ε_{yy} component predictions *vis-à-vis* ground truth. Based on these results, we conclude that the model fairly captures the strain details for this high-resolution image as well as the crack tip position. The ability of the model to predict for higher material resolution shows its capability to predict at multiple length scales.

Table 2. Comparison of FNO with ResNet and UNet

	R^2		L_2 Error	
Model	Stress (Mean ± SD)	Strain (Mean ± SD)	Stress	Strain
FNO	0.98 ± 0.07	0.99 ± 0.03	0.0896	0.0793
ResNet	0.96 ± 0.07	0.96 ± 0.03	0.1491	0.1830
UNet	0.93 ± 0.08	0.94 ± 0.03	0.1964	0.2175

We test the FNO, ResNet, and UNet for the same 200 test samples for both stress and strain predictions. In this table, we present the mean R^2 score and L_2 error metric. Both the metrics indicate the superior performance of FNO.

At times, we are interested in finer resolution details in the outputs, mainly around the stress concentrations or for the purpose of high-fidelity solutions. In classical solver setups such as FEM, we are required to take small mesh sizes to capture small-scale details. However, this imposes severe computational costs and makes such analysis inefficient. FNO's ability to transfer solutions across different resolutions puts it in a unique list of frameworks available that feature super-resolution functionality with tremendous speed up. In this case, we test the model for inputs having a fixed material grid size of 8 × 8 but varied overall image resolution. Figure 5B shows the vertical component (ε_{yy}) of strain predicted for (1) 104 × 104-size and (2) 200 × 200-size images along with AE plots. The model captures the strain patterns for both resolutions with decent accuracy. At points of stress concentration, the model suffers a bit because, in general, the DL models have the tendency to smoothen spikes (here stress concentrations) to lower the total loss. Overall, the ML model trained on lower-resolution data can be used to fetch results for a finer domain discretization with acceptable accuracy. With such performance, the results of the ML-based surrogate significantly reduce the costs of such analysis aimed at achieving high-precision results. Since the FNO model utilizes larger Fourier modes for feature training, this leads to the loss of small details. Therefore, one can increase the number of Fourier layers without dropping any Fourier modes to capture more sharp details but at the cost of computational efficiency.

Zero-shot generalization to unseen geometries

The real-world geometries of the composites can get complex having any type of material distribution. Therefore, to extend the ambit of our model, we test the model for arbitrary shapes. Earlier, the model has been trained on geometries with a chequerboard pattern of soft and stiff units; we now test it for geometries with arbitrary material distributions. These unseen geometries no longer have equal fractions of soft and stiff units, which was the case during model training. To demonstrate such a possibility, we prepare a test set with random uncheckered material geometries with similar FE settings as mentioned in the method details section. The geometries are created to represent wide complexities possible in the design paradigm of such composites. Herein, we provide the results for three typical arbitrary geometries in Figure 6. Since the composites are loaded in the horizontal direction (y-direction in FE setup), we evaluate the model for ε_{yy} component. It is quite evident that the model generalizes well to composites having complex shapes exhibiting an extraordinary performance for zero-shot predictions. From the above results, it can be concluded, in principle, the model has been able to learn the complex mechanical behavior without being provided with any knowledge of the underlying physics/mechanics. We no longer need different models for component-wise field quantity evaluations or different conditions be it the changing geometry, changing soft-stiff unit fractions, or finer material resolution. The versatility of the ML model to predict for a wide range of scenarios can be used to optimize different mechanical properties previously computationally inaccessible.

Von-mises stresses and equivalent strains

Until now, all the stress and strain components were directly outputted by the model. By using these results from the ML models, we aim to predict the equivalent quantities, specifically von-mises stress and equivalent strains. Von-mises stress is the nontensorial measure of stresses calculated using normal and shear components. Similarly, equivalent strain is an effective single-valued measure of strain components. The available studies use an end-to-end approach to calculate the equivalent quantities by training ML models to predict such quantities, citing the complexities in predicting multiple tensorial components in a single pass. However, our model has the capacity to predict multiple components, and hence, the equivalent measures of stresses and strains are computed by postprocessing the stress and strain tensor obtained using the trained FNO. Figure 7 shows the results for von-mises stress and equivalent strain distribution for a

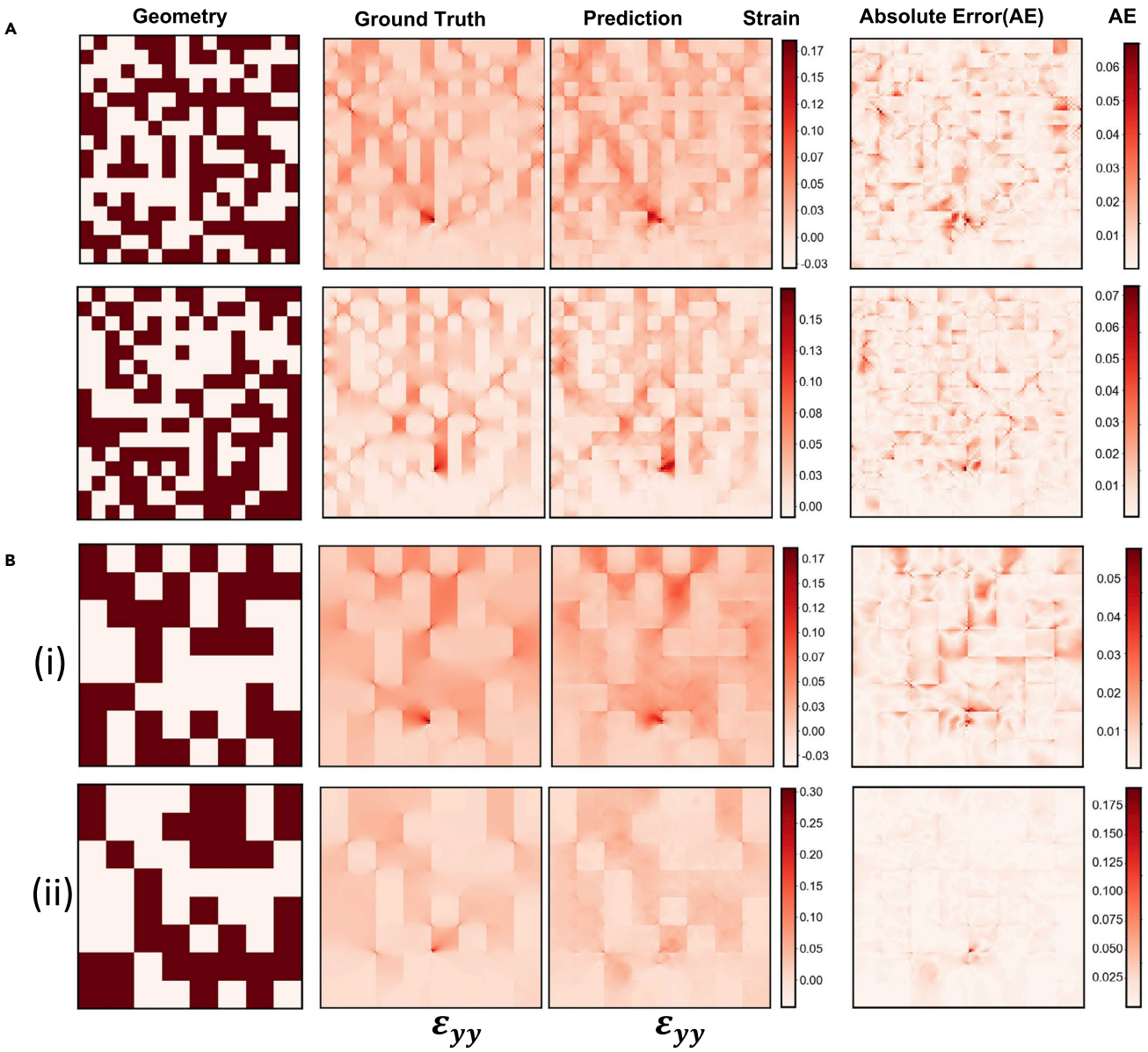

Figure 5. Super-Resolution

(A) Material-wise super-resolution: The model trained on geometric configurations with a 8 × 8 material grid is tested for the 16 × 16 material grid. Results are shown for two random geometric configurations along with AE distribution. Since loading is applied in the y-direction, the model is trained to predict the ε_{yy} component.

(B) Pixel-wise super-resolution: The model trained on 48 × 48 image resolution is used to predict solution for higher-resolution domains (1) 104 × 104 and (2) 200 × 200 image resolution. This establishes the robustness of the model with the ability to query solutions at new points in the domain.

typical digital 2D composite compared with the results from FEM. On analyzing the results, we find that both the quantities closely match the ground truth (FEM results), suggesting the model's capacity to recognize a complex material behavior. The robustness of the ML model to derive secondary mechanical quantities without the need to explicitly train for such can be used to evaluate the array of design settings leading to a composite with superior mechanical performance.

DISCUSSION

Altogether, in this study, we use a neural operator-based framework, FNO, to evaluate the mechanical response of digital composites subjected to tensile loading. To this extent, material geometries are

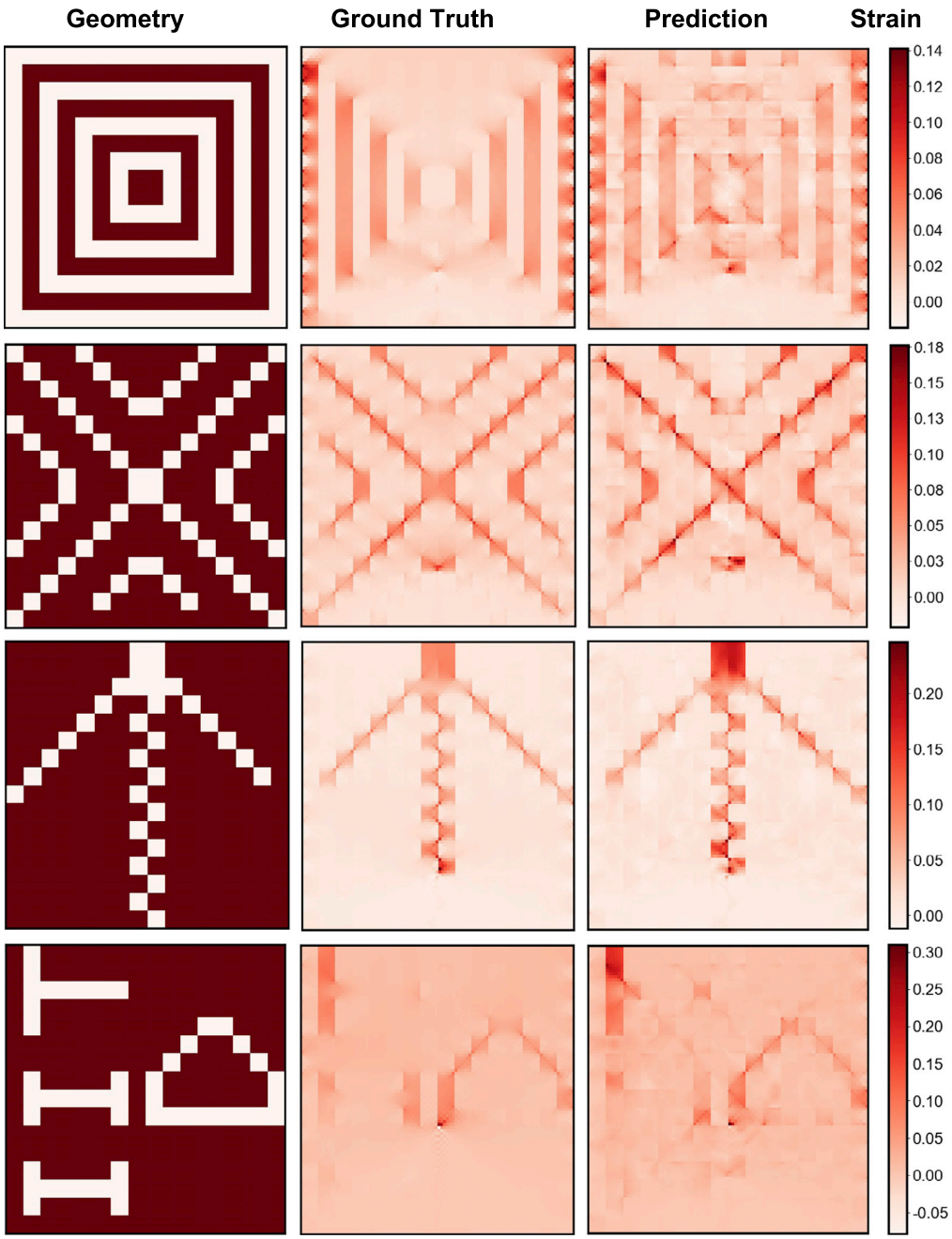

Figure 6. Zero-shot prediction for non-chequered material geometries

The model trained on chessboard geometry of soft and stiff units is tested against arbitrary uncheckered geometries with varying fractions of soft/stiff units. A direct comparison of ε_{yy} values of the ML model vs FEM shown for three typical examples.

randomly generated consisting of two distinct constituents of equal proportions. An end-to-end approach is used to predict the tensorial components of stress-strain fields. We show that the model trained on a fixed 48 × 48 resolution geometry images encoding material microstructure exhibits excellent agreement with the ground truth obtained from the FE simulations. Furthermore, we show that the FNO trained on a given resolution exhibits zero-shot generalizability to super-resolution both pixel-wise and material-wise. In addition, we show that the FNO exhibits zero generalizability to complex geometries with varying percentage of the constituent materials. Finally, FNO also provides excellent predictions for the

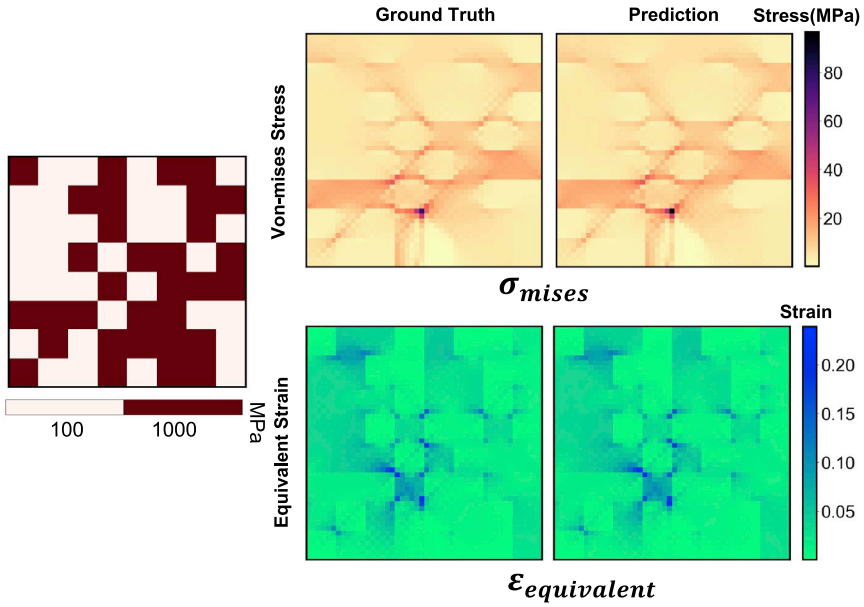

Figure 7. Measurement of equivalent stress-strain quantities

An end-to-end approach is used for this study to predict stress-strain tensorial components. Using these results to derive the equivalent stress and strain measures, viz, von-mises stress and equivalent strains. Distribution of these quantities is shown here for a typical geometry.

equivalent stresses and strains, allowing realistic upscaling of the results. These results substantiate the multifunctionality of the FNO model by generalizing over unknown microstructural shapes as well as outputting high-resolution predictions for low-resolution inputs.

Limitations of the study

At this juncture, it is worth mentioning some of the open challenges that remain to be addressed. Although the model provides excellent predictions in an overall fashion, the model exhibits inferior predictions for the stress concentrations at the crack tip, the improvement of which requires further work. Similarly, the crack propagation in the present work is modeled in a quasistatic fashion. Modeling dynamic fracture with varying time steps of integration remains an open challenge to be modeled in FNO. In addition, the ability of FNO to generalize to unseen boundary conditions remains to be explored. Finally, incorporating physics-based information to model the dynamics of crack propagation can be an interesting extension that can significantly enhance the performance of the model, while reducing the computational cost.

STAR★METHODS

Detailed methods are provided in the online version of this paper and include the following:

- KEY RESOURCES TABLE
- RESOURCE AVAILABILITY
  - Lead contact
  - Materials availability
  - Data and code availability
- METHOD DETAILS
  - Dataset preparation: Geometry, material properties, FE modelling
  - FE modelling
  - ML model and its training

SUPPLEMENTAL INFORMATION

Supplemental information can be found online at https://doi.org/10.1016/j.isci.2022.105452.

ACKNOWLEDGMENTS

Authors thank the High-Performance Computing (HPC) facility at IIT Delhi for computational and storage resources.

AUTHOR CONTRIBUTIONS

S.C. and N.M.A.K. supervised the work. M.M.R. contributed to data collection, processing, model training, and results and prepared the initial manuscript. T.P. and M.M.R. performed the FE simulations for dataset preparation. All the authors analyzed the results and edited the manuscript.

DECLARATION OF INTERESTS

The authors declare no competing interests.

INCLUSIONS AND DIVERSITY

We support inclusive, diverse and equitable conduct of research.

Received: July 19, 2022
Revised: October 1, 2022
Accepted: October 23, 2022
Published: November 18, 2022

REFERENCES

Barbero, E.J. (2017). Introduction to Composite Materials Design (CRC Press).

Bhaduri, A., Gupta, A., and Graham-Brady, L. (2022). Stress field prediction in fiber-reinforced composite materials using a deep learning approach. Compos. B Eng. *238*, 109879. https://doi.org/10.1016/j.compositesb.2022.109879.

Butler, K.T., Davies, D.W., Cartwright, H., Isayev, O., and Walsh, A. (2018). Machine learning for molecular and materials science. Nature *559*, 547–555. https://doi.org/10.1038/s41586-018-0337-2.

Chawla, R., and Sharma, S. (2018). A molecular dynamics study on efficient nanocomposite formation of styrene–butadiene rubber by incorporation of graphene. Graphene Technol. *3*, 25–33. https://doi.org/10.1007/s41127-018-0018-9.

Chen, P.-Y., McKittrick, J., and Meyers, M.A. (2012). Biological materials: functional adaptations and bioinspired designs. Prog. Mater. Sci. *57*, 1492–1704. https://doi.org/10.1016/j.pmatsci.2012.03.001.

Cui, Y., and Chew, H.B. (2022). Machine-learning prediction of atomistic stress along grain boundaries. Acta Mater. *222*, 117387. https://doi.org/10.1016/j.actamat.2021.117387.

Devlin, J., Chang, M.-W., Lee, K., and Toutanova, K. (2019). BERT: pre-training of deep bidirectional transformers for language understanding. In Proceedings of the 2019 Conference of the North American Chapter of the Association for Computational Linguistics: Human Language Technologies, Volume 1 (Long and Short Papers). Presented at the NAACL-HLT 2019 (Association for Computational Linguistics), pp. 4171–4186. https://doi.org/10.18653/v1/N19-1423.

Fedus, W., Zoph, B., and Shazeer, N. (2022). Switch transformers: scaling to trillion parameter models with simple and efficient sparsity. Preprint at arXiv. https://doi.org/10.48550/arXiv.2101.03961.

Ferreño, D., Sainz-Aja, J.A., Carrascal, I.A., Cuartas, M., Pombo, J., Casado, J.A., and Diego, S. (2021). Prediction of mechanical properties of rail pads under in-service conditions through machine learning algorithms. Adv. Eng. Software *151*, 102927. https://doi.org/10.1016/j.advengsoft.2020.102927.

Gu, G.X., Dimas, L., Qin, Z., and Buehler, M.J. (2016a). Optimization of composite fracture properties: method, validation, and applications. J. Appl. Mech. *83*. https://doi.org/10.1115/1.4033381.

Gu, G.X., Su, I., Sharma, S., Voros, J.L., Qin, Z., Buehler, M.J., and Buehler, M.J. (2016b). Three-dimensional-Printing of bio-inspired composites. J. Biomech. Eng. *138*, 021006. https://doi.org/10.1115/1.4032423.

Hanakata, P.Z., Cubuk, E.D., Campbell, D.K., and Park, H.S. (2020). Forward and inverse design of kirigami via supervised autoencoder. Phys. Rev. Res. *2*, 042006. https://doi.org/10.1103/PhysRevResearch.2.042006.

He, K., Zhang, X., Ren, S., and Sun, J. (2015). Deep Residual Learning for Image Recognition. https://doi.org/10.48550/arXiv.1512.03385.

Hughes, T.W., Williamson, I.A.D., Minkov, M., and Fan, S. (2019). Wave physics as an analog recurrent neural network. Sci. Adv. *5*, eaay6946. https://doi.org/10.1126/sciadv.aay6946.

Jensen, Z., Kim, E., Kwon, S., Gani, T.Z.H., Román-Leshkov, Y., Moliner, M., Corma, A., and Olivetti, E. (2019). A machine learning approach to zeolite synthesis enabled by automatic literature data extraction. ACS Cent. Sci. *5*, 892–899. https://doi.org/10.1021/acscentsci.9b00193.

Kadic, M., Milton, G.W., van Hecke, M., and Wegener, M. (2019). 3D metamaterials. Nat. Rev. Phys. *1*, 198–210. https://doi.org/10.1038/s42254-018-0018-y.

Kairn, T., Daivis, P.J., Ivanov, I., and Bhattacharya, S.N. (2005). Molecular-dynamics simulation of model polymer nanocomposite rheology and comparison with experiment. J. Chem. Phys. *123*, 194905. https://doi.org/10.1063/1.2110047.

Kim, B., Lee, S., and Kim, J. (2020). Inverse design of porous materials using artificial neural networks. Sci. Adv. *6*, eaax9324. https://doi.org/10.1126/sciadv.aax9324.

LeCun, Y., Bengio, Y., and Hinton, G. (2015). Deep learning. Nature *521*, 436–444. https://doi.org/10.1038/nature14539.

Li, Z., Kovachki, N., Azizzadenesheli, K., Liu, B., Bhattacharya, K., Stuart, A., and Anandkumar, A. (2020). Neural operator: graph kernel network for partial differential equations. Preprint at arXiv. https://doi.org/10.48550/arXiv.2003.03485.

Li, Z., Kovachki, N., Azizzadenesheli, K., Liu, B., Bhattacharya, K., Stuart, A., and Anandkumar, A. (2021). Fourier neural operator for parametric partial differential equations. Preprint at arXiv. https://doi.org/10.48550/arXiv.2010.08895.

Lim, J., Ryu, S., Kim, J.W., and Kim, W.Y. (2018). Molecular generative model based on conditional variational autoencoder for de novo molecular design. J. Cheminform. *10*, 31. https://doi.org/10.1186/s13321-018-0286-7.

Liu, R., Yabansu, Y.C., Agrawal, A., Kalidindi, S.R., and Choudhary, A.N. (2015). Machine learning approaches for elastic localization linkages in high-contrast composite materials. Integr. Mater. Manuf. Innov. *4*, 192–208. https://doi.org/10.1186/s40192-015-0042-z.

Liu, Y., and Zhang, X. (2011). Metamaterials: a new Frontier of science and technology. Chem. Soc. Rev. *40*, 2494–2507. https://doi.org/10.1039/C0CS00184H.

Lu, L., Jin, P., Pang, G., Zhang, Z., and Karniadakis, G.E. (2021). DeepONet: learning nonlinear operators for identifying differential equations based on the universal approximation theorem of operators. Nat. Mach. Intell. *3*, 218–229. https://doi.org/10.1038/s42256-021-00302-5.

Manual, A.U. (2014). Abaqus theory guide (Dassault Systèmes), p. 281. Version 6.

Meyers, M.A., Chen, P.-Y., Lin, A.Y.-M., and Seki, Y. (2008). Biological materials: structure and mechanical properties. Prog. Mater. Sci. *53*, 1–206. https://doi.org/10.1016/j.pmatsci.2007.05.002.

Meza, L.R., Das, S., and Greer, J.R. (2014). Strong, lightweight, and recoverable three-dimensional ceramic nanolattices. Science *345*, 1322–1326. https://doi.org/10.1126/science.1255908.

Meza, L.R., Zelhofer, A.J., Clarke, N., Mateos, A.J., Kochmann, D.M., and Greer, J.R. (2015). Resilient 3D hierarchical architected metamaterials. Proc. Natl. Acad. Sci. USA *112*, 11502–11507. https://doi.org/10.1073/pnas.1509120112.

Mozaffar, M., Bostanabad, R., Chen, W., Ehmann, K., Cao, J., and Bessa, M.A. (2019). Deep learning predicts path-dependent plasticity. Proc. Natl. Acad. Sci. USA *116*, 26414–26420. https://doi.org/10.1073/pnas.1911815116.

Nie, Z., Jiang, H., and Kara, L.B. (2019). Stress field prediction in cantilevered structures using convolutional neural networks. J. Comput. Inf. Sci. Eng. *20*. https://doi.org/10.1115/1.4044097.

Paszke, A., Gross, S., Massa, F., Lerer, A., Bradbury, J., Chanan, G., Killeen, T., Lin, Z., Gimelshein, N., Antiga, L., et al. (2019). PyTorch: An Imperative Style, High-Performance Deep Learning Library. https://doi.org/10.48550/arXiv.1912.01703.

Patel, R.G., Trask, N.A., Wood, M.A., and Cyr, E.C. (2021). A physics-informed operator regression framework for extracting data-driven continuum models. Comput. Methods Appl. Mech. Eng. *373*, 113500. https://doi.org/10.1016/j.cma.2020.113500.

Pathak, J., Subramanian, S., Harrington, P., Raja, S., Chattopadhyay, A., Mardani, M., Kurth, T., Hall, D., Li, Z., Azizzadenesheli, K., et al. (2022). FourCastNet: A Global Data-Driven High-Resolution Weather Model Using Adaptive Fourier Neural Operators. https://doi.org/10.48550/arXiv.2202.11214.

Pham, M.-S., Liu, C., Todd, I., and Lertthanasarn, J. (2019). Damage-tolerant architected materials inspired by crystal microstructure. Nature *565*, 305–311. https://doi.org/10.1038/s41586-018-0850-3.

Qin, Z., Yu, Q., and Buehler, M.J. (2020). Machine learning model for fast prediction of the natural frequencies of protein molecules. RSC Adv. *10*, 16607–16615. https://doi.org/10.1039/C9RA04186A.

Ramesh, A., Pavlov, M., Goh, G., Gray, S., Voss, C., Radford, A., Chen, M., and Sutskever, I. (2021). Zero-shot text-to-image generation. In Proceedings of the 38th International Conference on Machine Learning. Presented at the International Conference on Machine Learning (PMLR), pp. 8821–8831.

Ronneberger, O., Fischer, P., and Brox, T. (2015). U-net: convolutional networks for biomedical image segmentation. https://doi.org/10.48550/arXiv.1505.04597.

Senior, A.W., Evans, R., Jumper, J., Kirkpatrick, J., Sifre, L., Green, T., Qin, C., Žídek, A., Nelson, A.W.R., Bridgland, A., et al. (2020). Improved protein structure prediction using potentials from deep learning. Nature *577*, 706–710. https://doi.org/10.1038/s41586-019-1923-7.

Sepasdar, R., Karpatne, A., and Shakiba, M. (2021). A data-driven approach to full-field damage and failure pattern prediction in microstructure-dependent composites using deep learning. Preprint at arXiv. https://doi.org/10.48550/arXiv.2104.04485.

Stoll, A., and Benner, P. (2021). Machine learning for material characterization with an application for predicting mechanical properties. GAMM-Mitteilungen *44*, e202100003. https://doi.org/10.1002/gamm.202100003.

Su, I., Jung, G.S., Narayanan, N., and Buehler, M.J. (2020). Perspectives on three-dimensional printing of self-assembling materials and structures. Curr. Opin. Biomed. Eng. *15*, 59–67. https://doi.org/10.1016/j.cobme.2020.01.003.

Sun, Y., Hanhan, I., Sangid, M.D., and Lin, G. (2020). Predicting mechanical properties from microstructure images in fiber-reinforced polymers using convolutional neural networks. Preprint at arXiv. https://doi.org/10.48550/arXiv.2010.03675.

Wegst, U.G.K., Bai, H., Saiz, E., Tomsia, A.P., and Ritchie, R.O. (2015). Bioinspired structural materials. Nat. Mater. *14*, 23–36. https://doi.org/10.1038/nmat4089.

Xie, Q., Suvarna, M., Li, J., Zhu, X., Cai, J., and Wang, X. (2021). Online prediction of mechanical properties of hot rolled steel plate using machine learning. Mater. Des. *197*, 109201. https://doi.org/10.1016/j.matdes.2020.109201.

Yang, C., Kim, Y., Ryu, S., and Gu, G.X. (2020). Prediction of composite microstructure stress-strain curves using convolutional neural networks. Mater. Des. *189*, 108509. https://doi.org/10.1016/j.matdes.2020.108509.

Yang, Z., Yu, C.-H., and Buehler, M.J. (2021a). Deep learning model to predict complex stress and strain fields in hierarchical composites. Sci. Adv. *7*, eabd7416. https://doi.org/10.1126/sciadv.abd7416.

Yang, Z., Yu, C.-H., Guo, K., and Buehler, M.J. (2021b). End-to-end deep learning method to predict complete strain and stress tensors for complex hierarchical composite microstructures. J. Mech. Phys. Solid. *154*, 104506. https://doi.org/10.1016/j.jmps.2021.104506.

Zhang, X., Wang, Y., Ding, B., and Li, X. (2020). Design, fabrication, and mechanics of 3D micro-/nanolattices. Small *16*, 1902842. https://doi.org/10.1002/smll.201902842.

Zhou, K., Ma, W., Zeng, Z., Ma, X., Xu, X., Guo, Y., Li, H., and Li, L. (2019). Experimental and DFT study on the adsorption of VOCs on activated carbon/metal oxides composites. Chem. Eng. J. *372*, 1122–1133. https://doi.org/10.1016/j.cej.2019.04.218.

STAR★METHODS

KEY RESOURCES TABLE

REAGENT or RESOURCE	SOURCE	IDENTIFIER
Software and algorithms		
ABAQUS	Dassault Systèmes	Abaqus Unified FEA - SIMULIA™ by Dassault Systèmes® (3ds.com)
Data	Zenodo	https://zenodo.org/record/7127734
Code	Github	M3RG-IITD/FNO-StressStrain (github.com)

RESOURCE AVAILABILITY

Lead contact

Further information and requests for resources should be directed to and will be fulfilled by the lead contact, N. M. Anoop Krishnan (krishnan.@iitd.ac.in).

Materials availability

This study did not generate new materials.

Data and code availability

- Training data have been deposited at Zenodo: Learning the Stress-Strain Fields in Digital Composites using Fourier Neural Operator | Zenodo https://zenodo.org/record/7127734 and are publicly available as of the date of publication. DOIs are listed in the key resources table.
- The original code has been deposited at GitHub: https://github.com/M3RG-IITD/FNO-StressStrain and is publicly available as of the date of publication.
- Any additional information required to reanalyze the data reported in this paper is available from the lead contact upon request.

METHOD DETAILS

Dataset preparation: Geometry, material properties, FE modelling

Mode-I tensile test FE simulations are run on an 8 mm × 8 mm 2-D plate (thickness is taken to be negligible i.e. 0.001 mm compared to the other two dimensions and hence ignored to facilitate numerical compuatation) in ABAQUS (Manual, 2014) to generate the initial dataset for the FNO. We use an arbitrary composite material made up of two individual components, namely soft material and stiff material. The modulus ratio (E_{stiff}/E_{soft}) for the two materials is 10 while the failure stress for both is kept equal at an arbitrary value of 40 MPa. Consequently, the toughness ratio (G_{stiff}/G_{soft}) of the two materials is 0.1. The numerical values of material parameters are detailed in Table 1. Both the materials are assumed to be perfectly elastic, and a maximum principal stress criterion is used to define the point of damage initiation. The damage evolution (softening) criterion is based on the fracture energy (G). The square plate was divided into equal cells and each cell was assigned a material property (soft or stiff) randomly using a python script. However, the fraction of soft and stiff units is equal for all the FE samples. Therefore, each 2D composite has a material resolution of 8 × 8 and the overall image resolution is 48× 48. Each pixel corresponds to a finite element in the FE configuration. The loading is applied in the horizontal direction (global y-direction) and the pre-crack is along the x-direction. Around 1500 distinct configurations are generated and used for simulating mode-I tensile test for the composite plate using the above method. These configurations are randomly generated to explore a wide range of design arrangements. In addition to this, we generate multiple test sets with varied material and image resolution discussed in the results section. All the results are post-processed using ABAQUS's python interface which includes extracting nodal and elemental information (type of material, displacement, strain, stress etc.) from the FE simulations used for training and testing of the FNO model.

To define the boundary conditions (BCs) we label the sides of the input geometry as Left Edge(LE), Right Edge (RE) , Top Edge (TE) and Bottom Edge(BE) as shown in Figure 1. Also, U1 is the translational degree of freedom (DOF) along the x-axis, U2 is translational DOF in y-direction and UR3 is the z-direction rotational DOF . The loading is applied on the RE (y-direction). The LE has been fixed (U1 = U2 = UR3 = 0), and TE and BE have U1 = 0, U2 = free, UR3 = 0 as their BCs'.

FE modelling

The crack was modelled using Extended finite element method (X-FEM) which uses the partition of unity property of standard FE shape functions to add additional enrichment terms for modelling the displacement discontinuity. This eliminates the need of dynamic mesh refinement around the region of crack propagation and saves computational effort and time. The displacement field approximation for enriched nodes as per X-FEM is given as

$$u^h = \sum_{i \in I} u_i \varphi_i + \sum_{j \in J} b_j \varphi_j H(x) + \sum_{k \in K} \left(\sum_{l=1}^{4} c_k^l F_l(x) \right) \quad \text{Equation 6}$$

In the above equation, u^h represents the final displacement field, u_i represents the standard nodal displacement field, φ_i and φ_j are the shape functions, H(x) is the Heaviside function used to enrich the nodes along the crack path, $F_l(x)$ is the tip asymptotic function used to enrich the nodes near the crack tip (given in Equation 7), and b_j, c_k^l are additional degrees of freedom assigned to the enriched nodes. J is the jump displacement field for nodes along the crack front faces and K is the asymptotic displacement field near the crack tip.

$$F_l(r, \theta) = \sqrt{r} \sin\left(\frac{\theta}{2}\right), \sqrt{r} \cos\left(\frac{\theta}{2}\right), \sqrt{r} \sin\left(\frac{\theta}{2}\right) \sin(\theta), \sqrt{r} \cos\left(\frac{\theta}{2}\right) \sin(\theta) \quad \text{Equation 7}$$

A signed distance function is used as a level set function in ABAQUS to determine the nodes in the vicinity of the crack. The crack-line is treated as an intersection of two normal planes and the level set function is the signed distance of any point from the two planes. A general representation of enriched nodes using X-FEM in ABAQUS is shown in Figure S1. Finally, the direction of crack propagation is decided by the maximum principal stress criterion *i.e.*, the crack advances in the direction where the value of the principal stress is maximum.

ML model and its training

Model description

Neural Operators (NOs): Traditionally, neural networks have been used to learn the mappings between finite-dimensional Euclidean spaces. For such network constructs, we can only feed discrete inputs to learn the underlying relation under a typical supervised learning setting. Recently, a new paradigm has been established known as the neural operator (Li et al., 2020; Lu et al., 2021; Patel et al., 2021) to learn the mappings between infinite dimension Euclidean spaces. This generalization of neural network helps in learning the operator that maps input function space to solution space. We use these neural operators to solve the PDEs by specifically learning the operator that maps the input parameters $a \in \mathcal{A}$ to the solution space $u \in \mathcal{U}$. Let $D \subset \mathbb{R}^d$ be bounded and open set and $\mathcal{A} = (D; \mathbb{R}^{d_a})$ is the input function space, $\mathcal{U} = (D; \mathbb{R}^{d_u})$ is the output function space. $\mathcal{A}$ and $\mathcal{U}$ are the two Banach spaces of functions defined on domain D taking values in $\mathbb{R}^{d_a}$ and $\mathbb{R}^{d_u}$ respectively. $\mathcal{G}: \mathcal{A} * \theta \mapsto \mathcal{U}$ is the mapping that satisfies the PDE. Considering samples $\{a_j, u_j\}$ where a_j is an independent and identically distributed (i.i.d) sequence sampled from the probability measure μ in $\mathcal{A}$ and $u_j = \mathcal{G}(a_j)$, the neural operator approximates the mapping $\mathcal{G}_\theta$ by minimising the following stated problem using the cost function $C: \mathcal{U} \times \mathcal{U} \mapsto \mathbb{R}$

$$\min_\theta E_{a \sim \mu}[C(\mathcal{G}_\theta(a), \mathcal{G}(a))] \quad \text{Equation 8}$$

For the problem framework, we assume point-wise evaluations of both the input function a_j and solution function u_j. Let $D_j = \{x_1, x_2, \ldots, x_m\}$ be the m point discretization and a_j and u_j be the finite samples of input-output pairs accessible. In this computational setup, we work with these finite m pair data $\{a_j, u_j\}_{j=1}^m$ to learn the non-linear differential operator $\mathcal{G}_\theta$ which approximates the $\mathcal{G}: \mathcal{A} \mapsto \mathcal{U}$ satisfying the governing PDE.

Fourier Neural Operator: Using data-driven and physics-informed neural networks to satisfy the differential operator has significantly sped up the solution convergence in contrast to the classical PDE solvers.

However, these approaches become computationally expensive as they can only be trained for a single instance of PDE parameters $a \in \mathcal{A}$ and we require a different model training if the parameter setting is altered. To overcome this, the recently introduced Fourier Neural Operator is able to learn the non-linear differential operator which in turn learns the family of PDEs corresponding to different parameter values. Fourier Neural Operator is a state-of-the-art neural operator which can model a wide array of problems pertinent to the fields of fluid mechanics (Li et al., 2021) and climate modelling (Pathak et al., 2022). The architectural breakdown of FNO is shown in Figure 7. The input $a(x, t)$ is lifted to a higher dimension by fully connected shallow neural network P as $v(x); v(x) = P(a(x,t))$. This higher dimensional output is fed concurrently to an iterative setup of Fourier layer and convolution layer denoted as $v_{j+1} = \mathcal{H}(v_j)\ \forall\ j = 1, ..., T$ steps *on* $v_o(x)$. This typical update step is defined as

$$v_{j+1}(x) \cdot \sigma\left(Wv_j(x) + \left(\mathcal{K}(a;\varphi)v_j\right)(x)\right) \quad \forall x \in D \qquad \text{Equation 9}$$

where, $\sigma(\cdot) : \mathbb{R} \mapsto \mathbb{R}$ is a non-linear activation function, $W : \mathbb{R}^{d_v} \mapsto \mathbb{R}^{d_v}$ is a linear transformation, $\mathcal{K} : \mathcal{A} \times \theta \mapsto \mathcal{L}(\mathcal{U}, \mathcal{U})$ is the non-local integral operator. FNO treats $\mathcal{K}(a;\varphi)$ to be a kernel integral transformation parametrized by $\varphi \in \Theta_k$ k. This kernel integral operator is defined as:

$$\left(\mathcal{K}(v_j)(x)\right) = \int_D \kappa(a(x,y), x, y; \varphi)v_j(y)dy \quad x \in D\ ,\ j \in [1, T] \qquad \text{Equation 10}$$

where $\kappa_\varphi : \mathbb{R}^{2d+d_a} \mapsto R^{d_v \times d_v}$ is a neural network parametrized by $\theta \in \Theta$. It can be considered as the kernel function that is learned from the input data. By letting $\kappa(x,y) = \kappa(x - y)$, FNO replaces this kernel integral operator with a convolution operator defined in Fourier space where it is reduced to a basic multiplication operation. Let $\mathcal{F}$ denote the Fourier transform and $\mathcal{F}^{-1}$ the inverse Fourier transform, therefore (Equation 10) changes to

$$\left(\mathcal{K}(v_j)(x)\right) = \mathcal{F}^{-1}\left(\mathcal{F}(\kappa_\varphi) \cdot \mathcal{F}(v_j)\right)(x)\ )\ x \in D \qquad \text{Equation 11}$$

On parameterizing the κ directly by its Fourier coefficients, we get

$$\mathcal{K}(v)(x) = \mathcal{F}^{-1}\left(R_\varphi \times \mathcal{F}(v_j)\right)(x)\ x \in D \qquad \text{Equation 12}$$

where R_φ is the Fourier Transform of periodic function κ. On assuming κ as periodic, FNO exploits this by working with discrete Fourier modes of the Fourier expansion and truncates the series expansion at the maximum number of modes κ_{max} . The higher modes which are usually responsible for finer features are dropped to improve upon the speed of convergence as well as regularization. It is followed by an inverse Fourier transform to transform back to the spatial domain. The output of these iterative layers is fed to another shallow fully connected neural network which projects the data back to the target dimension. FNO takes advantage of the Fast Fourier Transform FFT algorithm to calculate the $\mathcal{F}$ and $\mathcal{F}^{-1}$ thereby responsible for its tremendous speed.

Model hyperparameters

The FNO architecture used for this study as described in Figure 7 comprises 6 layers in total. This includes 2 linear layers; one at the start and the other at the end having 32 and 128 nodes respectively and 4 Fourier layers in between. We train FNO by retaining the different number of modes and 12 modes are found to give the best results considering model accuracy and time needed during training. The model is trained on a single NVIDIA V100 GPU with 16GB memory using the PyTorch (Paszke et al., 2019) framework. We use a smoother version of ReLU namely GELU (Gaussian cumulative distribution function) activation function, ADAM optimizer which is a first order gradient-based method to train 500 epochs with a batch size of 20. We keep the weight decay as 10^{-4} and the initial learning rate is fixed at 0.001 and it halves after every 100 epochs (see Table S1). During the training, we use an L_2 based loss function which is defined as (Equation 5). The dataset is divided into 1200 training samples and 200 test samples. The above-stated values of batch size, learning rate, number of epochs and training set size have been considered after performing hyperparameter optimization.

Evaluation metrics

The output of the FE simulations is the element-wise data for each material geometry. The trained models are used to obtain the components of stress and strain tensors for material geometries having a unique configuration of soft and brittle units in their composition. Besides field variables, we evaluate global properties such as von-mises stresses and equivalent strain using the available field outputs. We present pixel to pixel comparison of the solutions obtained from the FNO model with those obtained from the numerical

solver. To quantitatively assess the performance of the FNO model, we measure element-wise absolute error (AE) maps and relative error (RE) for the field variables defined as:

$$AE: = \delta_{AE} = |\widehat{u}(x_i) - u(x_i)| \quad \text{Equation 13}$$

$$RE: = \delta_{RE} = \left|\frac{\widehat{u}(x_i) - u(x_i)}{u(x_i)}\right| \quad \text{Equation 14}$$

where $\widehat{u}(x_i)$ is the predicted value and $u(x_i)$ is the actual value for the *i-th* element. To compare the FNO with existing frameworks we calculate the R^2 and L_2 based metric as shown in Table 2. In addition to these, for every component, we plot the FEM vs prediction results for stress and strains along with specific cross-sectional directions. Among a wide range of available colour schemes, the colour spectrum used for plotting the results works best in terms of viewing the details at the soft and brittle interface as well as near the crack region.